Quantitative Imaging of Injectant Mole Fraction and Density in Supersonic Mixing

Hidemi Takahashi,* Shuzo Ikegami,* Hiroki Oso,* and Goro Masuya†
Tohoku University, Sendai 980-8579, Japan
and
Mitsutomo Hirota‡
Muroran Institute of Technology, Muroran 050-8585, Japan

The fluorescence ratio technique for processing planar laser-induced fluorescence data was generalized for quantitative imaging of the injectant mole fraction and extended to quantify the density distributions in a nonreacting supersonic mixing flowfield. The original fluorescence ratio approach was first developed by Hartfield et al. (Hartfield, R. J., Jr., Abbitt, J. D., III, and McDaniel, J. C., "Injectant Mole Fraction Imaging in Compressible Mixing Flow Using Planar Laser-Induced Iodine Fluorescence," *Optics Letters*, Vol. 1, No. 16, Aug. 1989, pp. 850–852.) for tests in a special closed-loop wind tunnel to eliminate the effects of thermodynamic property variations on planar laser-induced fluorescence signals in compressible flowfields. This approach provided us a quantitative means of planar mole-fraction measurement; however, it implicitly assumed that the tracer molecules were seeded at the same fraction in both the main and the secondary flows. In the present study, we generalized the Hartfield et al. method by considering differences in the tracer-seeding rates for obtaining planar images of mole fraction and density. Experimental validation of the new method was carried out in a mixing flowfield formed by sonic transverse injection into a Mach 1.9 supersonic airstream. The injectant mole-fraction distribution obtained from planar laser-induced fluorescence data processed by our new approach showed better agreement with the gas-sampling data than one based on the Hartfield et al. method. The density distribution was verified by comparison with the theoretical density ratio across the oblique shock wave.

Nomenclature

C	=	molar concentration, mol/m^3
c	=	velocity of light, m/s
D	=	diameter of injector, m
dV_c	=	optical-collection volume, cm^3
E	=	laser fluence, J/cm^2
H	=	tunnel height, mm
h	=	Planck's constant, $J \cdot s$
J	=	jet-to-freestream momentum flux ratio
k	=	Boltzmann constant, J/K
M	=	Mach number
m	=	molecular weight, kg/mol
N	=	number density, cm^{-3}
P	=	local pressure, Pa
R	=	gas constant, $J/(K \cdot mol)$
S	=	fluorescence signal intensity
T	=	local temperature, K
u	=	velocity, m/s
α	=	shock angle, rad
γ	=	specific heat ratio
η_{opt}	=	overall efficiency of collection optics
λ	=	excitation wavelength of laser, nm
ρ	=	density, kg/m^3
σ	=	molecular absorption cross section of excited molecules, cm^2
ϕ	=	fluorescence quantum yield of acetone
χ	=	mole fraction

Subscripts

ac_j	=	acetone seeding in the jet
ac_m	=	acetone seeding in the main flow
acetone	=	component of acetone
entire	=	jet and main flow
exit	=	flow condition at the jet exit
j (or jet)	=	jet
m (or main)	=	main flow
mixture	=	acetone/air mixture gas
ref	=	reference condition
uni	=	universal
0	=	stagnation condition
1	=	acetone seeding only in the jet
2	=	acetone seeding in both the jet and main flow

*Graduate Student, Department of Aerospace Engineering.
†Professor, Department of Aerospace Engineering. Senior Member AIAA.
‡Lecturer, Department of Mechanical Systems Engineering.

I. Introduction

QUANTITATIVE understanding of the mixing mechanism in a supersonic flowfield is vital for designing successful hypersonic propulsive devices represented by scramjet engines. The mixing feature is often characterized by such local flow properties as concentration and density, and so it is essential to measure those quantities accurately. In the supersonic mixing flowfields, measurement of concentrations as well as density with probes is quite difficult due to their high three-dimensional and complex features; hence, an optical diagnostic technique is preferable because of its nonintrusiveness.

Planar laser-induced fluorescence with acetone tracer (acetone PLIF) has been developed and has become popular for investigating gas concentrations in nonreacting compressible flows because of its excellent spatial and temporal resolution, strong fluorescence signal, and nonintrusiveness and because of the relative safety of the tracer to the human body and to the facility [1]. However, it is not possible to directly relate an image taken by PLIF to any physical quantity (e.g., concentration or density), because the fluorescence signal depends on both the mole fraction of tracer molecules and the local thermodynamic properties.

A fluorescence signal ratio approach introduced in [2] is quite useful in eliminating the thermodynamic dependencies of LIF signals, thus providing a quantitative means of mole-fraction measurement. The basic principle of this method is to take the ratio of two images recorded in two different seeding conditions (e.g., one for a tracer seeded only into the jet flow and the other for a tracer seeded into both the jet flow and the main flow). This approach makes it possible to cancel any nonuniformities in the collection optics as well as the thermodynamic dependencies. Though this technique is quite attractive, it is not clear whether or not this approach is applicable to configurations other than those of the Hartfield et al. fluorescence ratio method [2–7] (Hartfield method), as their experiments were conducted using a closed-loop wind tunnel in which the tracer-seeding levels of both flows were kept constant and equal during the entire experiment.

In the present work, we generalize the Hartfield method to apply it to other experimental setups and seeding conditions. The generalized fluorescence ratio method is verified by comparing the injectant mole-fraction distribution obtained by acetone PLIF with one obtained by gas-sampling in the flowfield of a sonic transverse injection into a Mach 1.9 supersonic airstream. In addition, we propose a new fluorescence-ratio-based method for imaging density distributions. We verify this method by comparing the density distributions obtained with the new method to the theoretical one across the oblique shock wave with a measured configuration. The important thing when using these generalized methods is to obtain the reference conditions of fluorescence signals and density. Once these reference conditions are obtained, this method is applicable to various flowfield with any complexity of shock systems.

II. Experimental Arrangements and Conditions

A. Wind Tunnel and Test Section

A schematic diagram of the present experimental apparatus is displayed in Fig. 1. A suction-type supersonic wind tunnel was used. Unheated atmospheric air was inhaled into a vacuum tank through a tracer-seeding section, a two-dimensional contoured nozzle of nominal Mach number 1.9, and a test section. The vacuum tank had a volume of 8 m³ and was evacuated to 5 kPa before each test run. The tracer-seeding section was an acrylic rectangular duct 100 mm wide, 100 mm high, and 400 mm long. A perforated plate was attached at the entrance of the section to enhance mixing of inhaled ambient air and acetone-seeded pressurized air. Five sheets of mesh and a bundle of straws used for rectification of air/acetone-mixture gas were set inside in the middle of this section. Compressed dry air from an air bomb was introduced into a bubbling container to vaporize the acetone and was then fed to the tracer gas injectors to seed acetone molecules as a tracer for LIF measurements in the main airstream. Another similar feeding line of the acetone/air mixture was directly connected to an injection port on the test section. The mole fraction of the seeded acetone was assumed to be well below the saturated condition at room temperature; the details will be discussed subsequently. The test section was a rectangular duct 30 mm wide, 30 mm high, and 200 mm long. A sonic transverse injector of 2.5 mm diameter was located on the centerline of the tunnel wall. Quartz glass windows were set on the three walls for optical access, enabling LIF measurements.

In this paper, the following Cartesian coordinate system was used. The origin was located at the center of the injector orifice. The streamwise axis was x, the transverse axis was y, and the spanwise axis was z.

B. PLIF Measurement

The light source used to induce acetone fluorescence was fourth-harmonic radiation from a Q-switched pulsed Nd:YAG laser with a wavelength of 266 nm, energy of 70 mJ/pulse, and a maximum repetition rate of 10 Hz. The laser beam was expanded into a two-dimensional sheet 30 mm wide and 0.5 mm thick. It was produced with six mirrors, two positive cylindrical lenses ($f = 200$ mm), and one negative cylindrical lens ($f = -20$ mm) so that the flowfield could be measured with a parallel light sheet. Given these laser sheet characteristics, the pulse energy of 70 mJ was well below the saturation level for acetone fluorescence. Mirrors were used to orient the sheet in the streamwise vertical (x–y) and spanwise vertical (y–z) planes.

The fluorescence images were recorded using a digital charge-coupled device (CCD) camera system with an image intensifier unit and a micro-Nikko 50 mm f2.8 lens. Operation of these devices was synchronized by a pulse generator. A bandpass filter (passband 390 ± 100 nm) was attached to the front of the camera lens to block stray light. MATLAB 7.1 software was used for postprocessing.

C. Gas-Sampling Measurement

Figure 2 illustrates the test section used for the gas-sampling experiments. It had the same cross section as that used for the LIF measurement but was 130 mm longer. All of the walls except for the injector wall were made of clear acrylic resin. A three-point gas-sampling probe rake was inserted through a port on the wall opposite the injector wall. The probe rake could be moved in the x direction from 5 to 30 mm at intervals of 5 mm and in the y direction from 3 to 14 mm. Each sampling probe had an outer diameter of 0.88 mm and an inner diameter of 0.58 mm at the tip. The distance between the probes was 3 mm. The blockage ratio of the probe rake parts to the tunnel cross section was 0.34%, which is an acceptable value for avoiding an unstart of the wind tunnel. The injector diameter D was 2.8 mm in this experiment. The diameter of the gas-sampling test section differed from that in the LIF measurement, due to inaccuracy
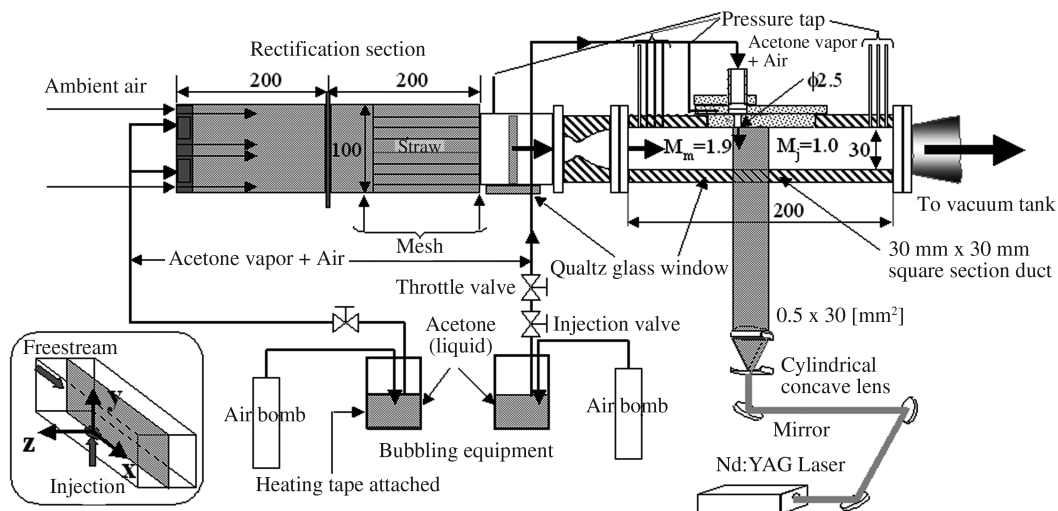

Fig. 1 Schematic diagram of the test facility.
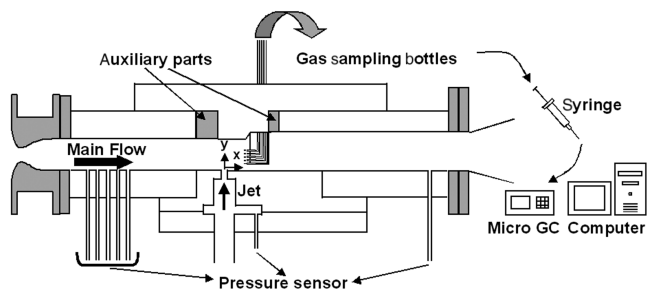
Fig. 2   Test section for gas-sampling.

in manufacturing. Therefore, the length in each test section was nondimensionalized by each injector diameter to cancel out any effects resulting from the difference in diameter. To obtain a sufficient amount of sampling gas in the cases of low pitot pressure, 8 s were required for sampling line scavenging and 12 s were required for gas-sampling. The sampling points are indicated in Fig. 3. Gaseous nitrogen was used as an injectant.

Figures 4a and 4b are schlieren photographs of the flowfields without and with the sampling probes. As seen here, inserting the probes caused no remarkable changes in the flow structure around the jet. In addition, no strong interaction between the shock waves from the probes and the boundary layer was observed.

D.   Flowfield Conditions and Acetone Addition Rates

The flowfield conditions are summarized in Table 1. We measured the total pressure and temperature for both the jet and the main flow. The static pressures and temperatures for both the jet and the main flow were derived from using the isentropic relationship with their measured stagnation conditions, Mach numbers, and gas properties. The jet-to-main-stream momentum flux ratio J was determined by use of the preceding quantities and the following derived equation:

Fig. 3   Sketch of the measurement points for gas-sampling.

a)

b)

Fig. 4   States of the flowfield pictured by schlieren photographs in the case of gas-sampling.

Table 1   Flowfield conditions

Condition	Main	Jet
Total pressure, kPa	75.0 ± 1.2	136.0 ± 2.5
Total temperature, K	291.0 ± 3	291.0 ± 3
Static pressure, kPa	11.2 ± 0.2	71.9 ± 1.3
Static temperature, K	169.0 ± 1.7	242.5 ± 2.5
Flow rate, g/s	94.8 ± 1.0	1.58 ± 0.02
Mach number	1.9	1.0

$$J = \frac{(\gamma p M^2)_j}{(\gamma p M^2)_m} = \left(\frac{\gamma_j}{\gamma_m}\right) \cdot \left(\frac{M_j^2}{M_m^2}\right) \cdot \left(\frac{p_{0j}}{p_{0m}}\right)$$

$$\cdot \left\{ \frac{(1 + [(\gamma_j - 1)/2]M_j^2)^{-\frac{\gamma_j}{\gamma_j-1}}}{(1 + [(\gamma_m - 1)/2]M_m^2)^{-\frac{\gamma_m}{\gamma_m-1}}} \right\} \qquad (1)$$

Here, we assumed that the specific heat ratio in both the jet and the main flow were the same as $\gamma_j = \gamma_m = 1.4$. The Mach number of the jet was unity because the flow is supposed to be choked at the injector orifice. The Mach number of undisturbed main stream was obtained from particle image velocimetry measurement separately conducted. The resulting value of J was fixed at 1.87 ± 0.07 throughout this study.

We assessed the effect of acetone addition on the physical properties of air by rough estimation of the addition rate. The addition rate of acetone into air was estimated with the assumption that the acetone molecule was uniformly mixed with air well below saturation, which was calculated by using the equation of saturated vapor pressure of acetone [8]. The estimated saturation level of acetone for the jet at the injector exit condition was 2.3% at the maximum, with assumptions of isentropic expansion from the stagnation conditions tabulated in Table 1 in the throat and with the use of the law of partial pressure. Because we did not observe any condensation of acetone vapor after injection, the seeding rate was kept at less than 2.3% that is the saturation level at the injector exit. For the main flow, the addition rate was estimated in the following way to be 0.7%: In the bubbling container, acetone was pressurized at 400 kPa and heated to 323 K, then the saturated acetone vapor was uniformly mixed into the pressurized air from the air bomb. At this time, the addition rate could be estimated at 20%. The acetone/air mixture was then injected into the rectification section and diluted to 1/30 by inhaled atmospheric air. These addition rates resulted in an air density change of 1.0% at the most. Therefore, introducing this level of acetone seeding had a negligible influence on the estimation of the injectant mole fraction.

The fluorescence fluctuations were measured to verify the uniformity of the inlet flow and acetone seeding in the main stream. The intensity of spatial fluctuation of the fluorescence signal was measured on a line across the exit of the Laval nozzle. The level of fluctuation was on the order of 2%, resulting in a 2% level of characteristic fluctuation in the jet-to-freestream momentum flux ratio, due to the change in molecular weight of the main stream: an acceptable level for the present experiment.
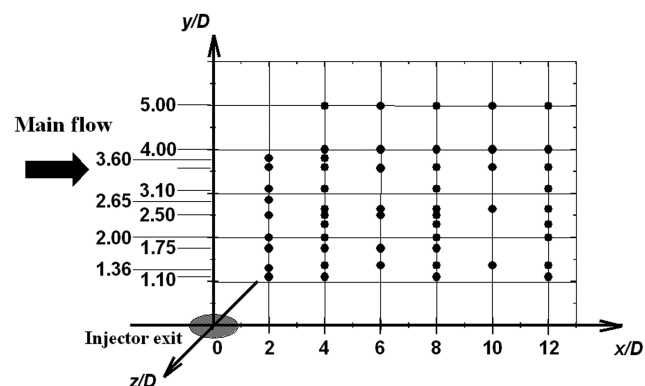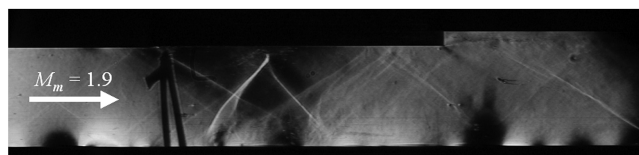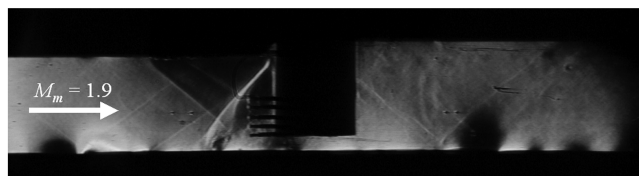
E.   Uncertainty Analysis

For the LIF measurement, the total uncertainty inherent in each fluorescence data point, associated with the elements of error sources tabulated in Table 2, was estimated to be 4.1%. Taking the square root of the sum of the squares of each source yielded an overall uncertainty of 4.1% in the LIF measurement. This number translated directly into a relative fluorescence uncertainty of the same amount, which was consistent in magnitude with the degree of repeatability observed for the same fluorescence experiment repeated at different times.

For the gas-sampling measurement, errors were considered to be induced by random uncertainties and systematic error (Table 2). The random uncertainties were determined by the repeatability for each measurement. The systematic error was dominated by the deviation in the calibration. We carried out calibration experiments several

Table 2 Uncertainty estimates in LIF and gas-sampling measurement

Measurement	Error source	Uncertainty, %
LIF	Shot noise	1.6
	Deviation of acetone seeding	2.00 (jet)
		1.59 (main)
	Regulated pressure variance	1.87 (jet)
		1.59 (main)
	Temperature variance	1.02
	Total uncertainty	4.1%
Gas-sampling	Random error	4.5
	Systematic error	2.0
	Total uncertainty	4.9%

times and found no day-to-day variation. Therefore, the main factor in the error was the determination process for the best-fitting calibration curve, and the value was 2.0%. Taking the square root of these elements, the overall error was estimated to be 4.9%. In low-pitot-pressure regions (e.g., the recirculation zone immediately downstream from the injector and near the wall), the error level was relatively large and could reach 10%.

In summary, we found 4.1% uncertainty in the LIF measurement and 4.9% uncertainty in the gas-sampling measurement. With regard to the uncertainty in Hartfield et al.'s [7] experiments, they estimated overall uncertainty for obtaining the injectant mole fraction by LIF measurement to be around 2 to 3%. Although the uncertainty in this study is a bit greater than that of Hartfield et al.'s study, it can be considered as an acceptable level.

III. Generalization of Fluorescence Ratio Method

A. Injectant Mole Fraction

Fluorescence from acetone molecules with broadband absorption spectra is affected by the temperature, pressure, and mole fraction of the irradiated acetone species. The acetone LIF intensity S, in number of photons collected, is modeled as Eq. (2), assuming linearity in the fluorescence signal, an excitation energy much lower than the saturation energy of the molecules, negligible laser beam attenuation, and negligible radiation trapping [9,10]:

$$S = \eta_{opt} \frac{E}{hc/\lambda} \, dV_c \sigma(\lambda, T) \phi(\lambda, T, P) \left[\frac{\chi_{acetone} P}{kT} \right] \quad (2)$$

The bracketed term on the right-hand side of Eq. (2) designates the number density of the acetone molecules; hence, it is clear that fluorescence intensity is proportional to the product of the local number density of the fluid and the mole fraction of the irradiated acetone species. However, in a compressible mixing flowfield, it is impossible to derive the acetone mole fraction directly from the LIF signal without some additional assumptions because all thermodynamic variables of a fluid may vary simultaneously and independently, as the mole fraction of the fluid component does.

According to Takahashi et al. [11], the fluorescence signal S can be expressed as a function of the acetone molar concentration $C_{acetone}$ (mol/m^3) in the following form:

$$S = \eta_{opt} \frac{E}{hc/\lambda} \cdot dV_c \cdot \frac{R_{uni}}{k} \cdot \phi(\lambda, T, P) \cdot C_{acetone} \quad (3)$$

$$C_{acetone} = \frac{\chi_{acetone} \cdot \rho_{mixture}}{m_{mixture}} = \chi_{acetone} \cdot N_{mixture} \cdot \frac{k}{R_{uni}} \quad (4)$$

Here, Eq. (3) regards the absorption cross section as constant by following Kashitani et al.'s results [12] that the absorption cross section is almost constant when excited at 266 nm and below the normal pressure range. The fluorescence quantum yield is calculated by the way described in [10]. The estimated maximum error of ±6% over the entire flowfield is included when converting the

fluorescence signal to molar concentration with calculated conditions of 0.1 atm $\leq P \leq$ 1.0 atm, 100 K $\leq T \leq$ 300 K, and 0% $\leq \chi_{acetone} \leq$ 100%.

Using the previously mentioned relationships, we related the fluorescence intensities obtained in the two seeding conditions illustrated in Fig. 5 as follows: When only the injectant jet is seeded with acetone, the fluorescence signal is proportional to the number density of the acetone fed by the jet. When both the jet and the main flow are seeded, the fluorescence signal is proportional to the sum of the acetone number density fed by the jet $\chi_{ac_j} N_j$ and that by the main flow $\chi_{ac_m} N_m$. If the acetone is uniformly mixed in each flow, the acetone number density is related to the entire number density of the seeded source N_{entire} by

$$\chi_{acetone} N_{entire} = \chi_{ac_j} N_j + \chi_{ac_m} N_m$$
$$\chi_{ac_j} N_j = \chi_{ac_j} \chi_j N_{entire} \quad (5)$$
$$\chi_{ac_m} N_m = \chi_{ac_m} (1 - \chi_j) N_{entire}$$

If the same laser sheet and optical-collection geometries are used in the measurements of both seeding conditions, the terms regarding the collection optics are canceled. Taking these facts into account and using Eqs. (3–5), we obtain the following expressions for the acetone fluorescence signals. In the case of jet-only seeding (case 1),

$$S_1 \propto \chi_{ac_{j1}} N_j = \chi_{ac_{j1}} \chi_j N_{entire} \quad (6)$$

In the case of entire-flow seeding (case 2),

$$S_2 \propto \chi_{ac_{j2}} N_j + \chi_{ac_{m2}} N_m = \{\chi_{ac_{j2}} \chi_j + \chi_{ac_{m2}}(1 - \chi_j)\} N_{entire} \quad (7)$$

Dividing the image acquired in case 1 by that acquired in case 2, the resulting ratio of fluorescence signals is related to the injectant mole fraction χ_j by the following equation:

$$\frac{S_1}{S_2} = \frac{\chi_{ac_{j1}} \chi_j}{\chi_{ac_{j2}} \chi_j + \chi_{ac_{m2}}(1 - \chi_j)} \quad (8)$$

Rearranging this equation, we obtain an explicit equation for the injectant mole fraction:

$$\chi_j = \frac{\chi_{ac_{m2}}/\chi_{ac_{j2}}}{[(\chi_{ac_{m2}}/\chi_{ac_{j2}}) - 1] + (S_2/S_1)(\chi_{ac_{j1}}/\chi_{ac_{j2}})} \quad (9)$$

The value of $\chi_{ac_{j1}}/\chi_{ac_{j2}}$ is a constant used to correct the slight difference in the acetone seeding rates into the jet for the two cases. The constant $\chi_{ac_{m2}}/\chi_{ac_{j2}}$ is derived in the following way. In this study, we deal with only gaseous flows, so that the ratio of the seeding rates of the jet and main flow is equal to the ratio of the mole fractions of acetone seeded in the two flows. Taking these facts into account and using Eqs. (3) and (4), we obtain the following relationship:

$$\left(\frac{\chi_{ac_{m2}}}{\chi_{ac_{j2}}} \right) = \left[\left(\frac{S_j}{S_m} \right) \left(\frac{\rho_m}{\rho_j} \right) \right]_{ref} \quad (10)$$

The right-hand side of Eq. (10) is determined by the measured or known values at the reference points. Here, S_j, the fluorescence intensities at the injector orifice, and S_m, those at the main flow region, are evaluated with those at the corresponding points in the
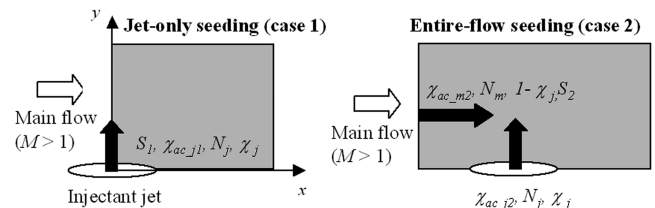
Fig. 5 Schematic diagram of a simplified model of acetone seeding methods in a flowfield of interest.

image of case 2. The values of ρ_j and ρ_m at the reference points are derived from the stagnation conditions and the isentropic relationships for the injection orifice and the inlet of the test section. We then obtained the following equation for χ_j:

$$\chi_j = \left[\left(\frac{S_j}{S_m}\right)\cdot\left(\frac{\rho_m}{\rho_j}\right)\right]_{\text{ref}} \bigg/ \left\{\left[\left(\frac{S_j}{S_m}\right)\cdot\left(\frac{\rho_m}{\rho_j}\right)\right]_{\text{ref}} - 1 \right.$$
$$\left. + \left(\frac{S_2}{S_1}\right)\left(\frac{\chi_{\text{ac}_{j1}}}{\chi_{\text{ac}_{j2}}}\right)\right\} \tag{11}$$

From Eq. (9), it is obvious that the value of χ_j varies with $\chi_{\text{ac}_{m2}}/\chi_{\text{ac}_{j2}}$ as well as with S_2/S_1. Figure 6 plots the dependence of injectant mole fraction χ_j on $\chi_{\text{ac}_{m2}}/\chi_{\text{ac}_{j2}}$. The important point here is that the value of χ_j for a given S_2/S_1 varies greatly with $\chi_{\text{ac}_{m2}}/\chi_{\text{ac}_{j2}}$. The Hartfield method, expressed by Eq. (12), corresponds to a special case in which $\chi_{\text{ac}_{m2}}/\chi_{\text{ac}_{j2}}$ equals unity:

$$\chi_j = \frac{\chi_{\text{ac}_{j2}}}{\chi_{\text{ac}_{j1}}}\cdot\frac{S_1}{S_2} \quad \text{for} \quad \frac{\chi_{\text{ac}_{m2}}}{\chi_{\text{ac}_{j2}}} = 1 \tag{12}$$

For $\chi_{\text{ac}_{m2}}/\chi_{\text{ac}_{j2}}$ other than unity, we need to use Eq. (9) to obtain the injectant mole-fraction distribution from the PLIF data.

B. Density

The fluorescence signal is proportional to both the acetone mole fraction and the local density of the mixture gas. Therefore, if the injectant mole fraction χ_j is known, the local density of the mixture gas ρ_{mixture} composed of jet and main flow can be derived. Expressing case 2 in the different form of Eq. (7),

$$S_2 \propto \frac{\rho_{\text{mixture}}\cdot\chi_{\text{mixture}}}{m_{\text{mixture}}}\cdot\phi_{\text{mixture}} = \rho_{\text{mixture}}\cdot\phi_{\text{mixture}}$$
$$\cdot\frac{\chi_j\cdot\chi_{\text{ac}_{j2}} + (1-\chi_j)\cdot\chi_{\text{ac}_{m2}}}{\chi_j\cdot m_j + (1-\chi_j)\cdot m_m} \tag{13}$$

Rearranging this equation with respect to ρ_{mixture},

$$\rho_{\text{mixture}} \propto S_2\cdot\left[\frac{1/\chi_{\text{ac}_{j2}}}{\chi_j + (1-\chi_j)\cdot(\chi_{\text{ac}_{m2}}/\chi_{\text{ac}_{j2}})}\right]\cdot\frac{m_{\text{mixture}}}{\phi_{\text{mixture}}} \tag{14}$$

Considering the reference condition at the injector exit,

$$\rho_{\text{mixture,exit}} \propto S_{2,\text{exit}}\cdot\left[\frac{1/\chi_{\text{ac}_{j2}}}{\chi_{j,\text{exit}} + (1-\chi_{j,\text{exit}})\cdot(\chi_{\text{ac}_{m2}}/\chi_{\text{ac}_{j2}})}\right]$$
$$\cdot\frac{m_{\text{mixture,exit}}}{\phi_{\text{mixture,exit}}} \tag{15}$$

Dividing Eq. (14) by Eq. (15) to cancel out the unknown term $1/\chi_{\text{ac}_{j2}}$, and then combining the relations of
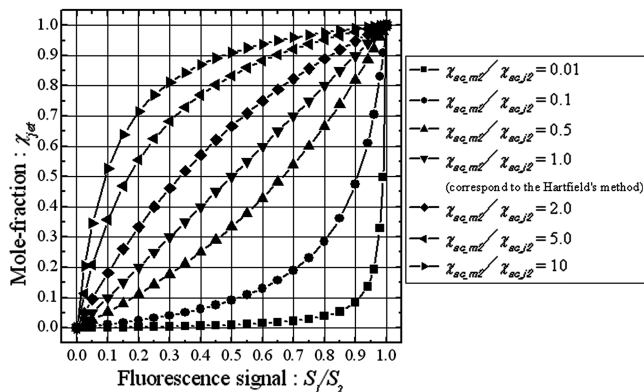

Fig. 6 Variation in mole fraction against fluorescence signal with the change of $\chi_{\text{ac}_{m2}}/\chi_{\text{ac}_{j2}}$.

$$\left(\frac{\chi_{\text{ac}_{m2}}}{\chi_{\text{ac}_{j2}}}\right)_{\text{ref}} \approx \left(\frac{S_{m2}}{S_{j2}}\cdot\frac{\rho_{j2}}{\rho_{m2}}\right)_{\text{ref}}$$

and $\chi_{j,\text{exit}} = 1$, we obtain an explicit equation for the normalized local density of the mixture gas:

$$\frac{\rho_{\text{mixture}}}{\rho_{\text{mixture,exit}}} = \left(\frac{S_2}{S_{2,\text{exit}}}\right)\cdot\left\{1\bigg/\left[\chi_j + (1-\chi_j)\cdot\left(\frac{S_{m2}}{S_{j2}}\cdot\frac{\rho_{j2}}{\rho_{m2}}\right)_{\text{ref}}\right]\right\}$$
$$\cdot\left(\chi_j + (1-\chi_j)\cdot\frac{m_m}{m_j}\right)\cdot\left(\frac{\phi_{\text{mixture,exit}}}{\phi_{\text{mixture}}}\right) \tag{16}$$

The change in molecular weight due to acetone seeding is negligible in the present experiment; hence, $m_m/m_j \approx 1$. Therefore, Eq. (16) reduces to the following equation:

$$\frac{\rho_{\text{mixture}}}{\rho_{\text{mixture,exit}}} = \left(\frac{S_2}{S_{2,\text{exit}}}\right)\cdot\left\{1\bigg/\left[\chi_j + (1-\chi_j)\cdot\left(\frac{S_{m2}}{S_{j2}}\cdot\frac{\rho_{j2}}{\rho_{m2}}\right)_{\text{ref}}\right]\right\}$$
$$\cdot\left(\frac{\phi_{\text{mixture,exit}}}{\phi_{\text{mixture}}}\right) \tag{17}$$

The reference values given in the bracketed term in the denominator are derived from a method similar to that explained in the mole-fraction measurement. The term related to the quantum fluorescence yield $\phi_{\text{mixture,exit}}/\phi_{\text{mixture}}$ is also calculated based on their thermodynamic conditions and the way described in [10]. The change of this term under the present experimental conditions is within 1%, and it results in a maximum 1% error in the density ratio, because the density ratio is multiplied by the fluorescence quantum ratio; hence, if we accept the 1% error, Eq. (17) can be reduced to

$$\frac{\rho_{\text{mixture}}}{\rho_{\text{mixture,exit}}} = \left(\frac{S_2}{S_{2,\text{exit}}}\right)\cdot\left\{1\bigg/\left[\chi_j + (1-\chi_j)\cdot\left(\frac{S_{m2}}{S_{j2}}\cdot\frac{\rho_{j2}}{\rho_{m2}}\right)_{\text{ref}}\right]\right\} \tag{18}$$

For the case of $\chi_{\text{ac}_{m2}}/\chi_{\text{ac}_{j2}}$ equals unity, corresponding to the Hartfield method, Eq. (18) reduces to

$$\frac{\rho_{\text{mixture}}}{\rho_{\text{mixture,exit}}} = \frac{S_2}{S_{2,\text{exit}}} \quad \text{for} \quad \frac{\chi_{\text{ac}_{m2}}}{\chi_{\text{ac}_{j2}}} = 1 \tag{19}$$

In this case, it is easy to obtain the density distribution in the entire flowfield because the fluorescence intensity distribution in case 2 directly corresponds to the density distribution. To conclude the density measurement, if we carry out PLIF experiments in cases 1 and 2, we can obtain the absolute density distribution.

IV. Results and Discussion

A. Flow Visualization by Acetone PLIF

Figures 7a and 7b are mean fluorescence images obtained from 300 instantaneous frames in the center plane of the test section for the jet-only and entire-seeding conditions. In each image, background scattered noise was subtracted and the nonuniformity of the laser sheet intensity was corrected. The flowfield near the opposite wall was masked in the image because of strong noise due to reflection of the laser sheet from the wall. The influence of reflection appeared as far as about 3 jet diameters from the opposite wall, which corresponds to one-quarter of the tunnel height ($y_{\text{masked}}/H = 1/4$). If this kind of optical-based experiment is conducted with an open flowfield without an opposite wall (such as described in [13]), this matter will not occur. In the image for jet-only seeding, the fluorescence signal varies with changes in both the injectant mole fraction and the local density and represents the distributions of the jet molar concentration. In Fig. 7b for the entire seeding, typical flow features [i.e., bow shock wave (A), barrel shock wave (B), Mach disk (C), recompression shock wave (D), and recirculation region (E)] are clearly seen. The strong density dependence of the fluorescence signal is evident in the large variation in signal intensity across the bow shock wave induced by injection.
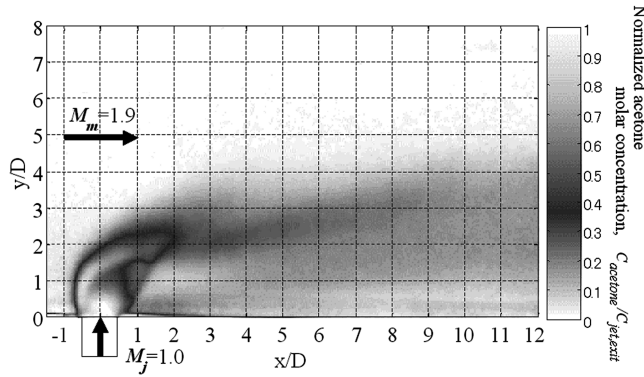
a) Jet-only seeded image (case 1)
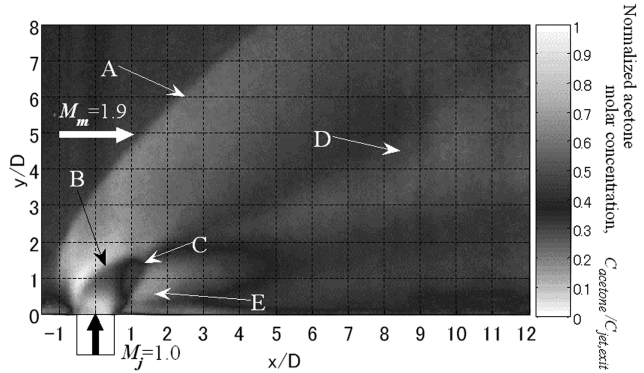
b) Entire flowfield seeded image (case 2)

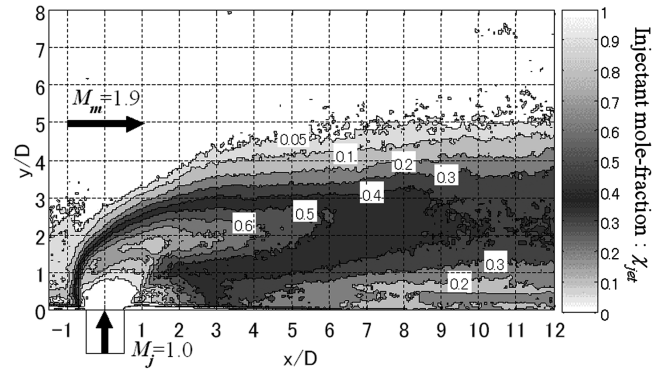Fig. 7   Mean images of acetone PLIF in the center plane.

a) Based on the Hartfield method

b) Based on the present method

Fig. 8   Injectant mole-fraction distribution in the center plane obtained by the fluorescence ratio methods.

B.   Injectant Mole-Fraction Distributions

Figure 8a depicts the ratio of the images in Figs. 7a and 7b with the measured value of $\chi_{\mathrm{ac}_{j1}}/\chi_{\mathrm{ac}_{j2}}$ in Eq. (12). Each contour spans 10% intervals from 10 to 100%, and 5% bands are plotted as well. If we were to adopt the Hartfield model, this image would represent the injectant mole-fraction distribution. In this study, however, the value of $\chi_{\mathrm{ac}_{m2}}/\chi_{\mathrm{ac}_{j2}}$ determined from the results of five independent experiments was not unity, but 0.45 ± 0.10. Therefore, Fig. 8a does not represent the correct mole-fraction distribution.

Figure 8b plots the injectant mole-fraction distribution derived from the images of Figs. 7a and 7b using Eqs. (10) and (11). A comparison of Figs. 8a and 8b reveals that the Hartfield method overestimates the mole fraction of injectant and thus the penetration height of jet in this case of $\chi_{\mathrm{ac}_{m2}}/\chi_{\mathrm{ac}_{j2}} = 0.45$. In Fig. 8b, the core of the jet for which the injectant has not mixed with air, yet exists at the injection port, but its shape is not clear. The mixing region begins outside the jet core and extends into both the jet core and the main airstream. Air diffuses into the jet before the jet passes through the Mach disk. Moreover, the mixing region extends to 1 jet diameter upstream of the jet. The distance to achieve an injectant mole fraction of 0.3, which is a stoichiometric value for hydrogen (supposed to be a scramjet fuel) in air takes 7 jet diameters downstream of the jet exit, with the penetration height of 3 jet diameters.

Figure 9 plots the maximum mole-fraction distribution against the nondimensional streamwise distance in $1.0 \le x/D \le 10$ on a log–log scale. The maximum mole fraction declines along the line of $\chi_j \approx (x/D)^{-0.62}$ until it reaches $x/D = 10$, then it decreases more slowly. This declining rate is close to those previously reported [14–16]. The tendency of the maximum mole-fraction distribution in the further downstream region was not clear because of the limited observation area.

Figure 10 compares PLIF and gas-sampling data for the injectant mole-fraction profiles at $x/D = 4$ in the center plane. Because the injector diameters were not the same in the two experiments, the comparison was made at the same nondimensional distance from the injector normalized by each injector diameter. In Fig. 10, the dashed line represents the PLIF data processed with the Hartfield method,
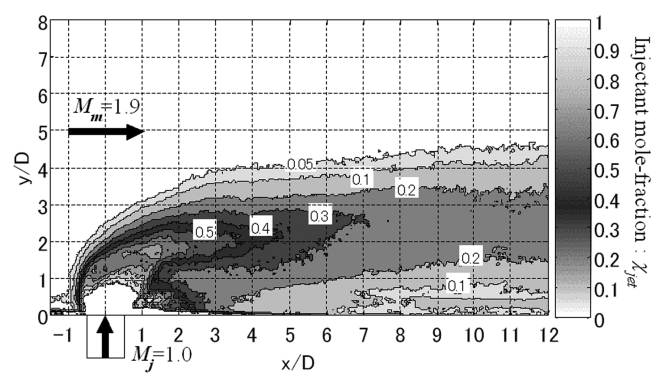
the solid line represents data processed with the generalized method developed in this study, and the circles represent the gas-sampling data. The gas-sampling data exhibit better agreement with the solid line than with the dashed line. Figure 11 is a combined plot of the gas-sampling data profiles at $x/D = 2, 4, 6, 8, 10$, and 12, along with the generalized PLIF distribution obtained with the present method. The generalized PLIF profiles and the gas-sampling data agree well over the entire region, except for the portion near the bottom wall, on which we observed large errors in the PLIF due to light scattered by the wall and errors in the gas-sampling due to the extremely low pitot pressure.

Figure 12 presents an overall comparison of the mole fractions obtained from the PLIF data and those obtained from the gas-sampling data to verify the universality of the present method. The solid black line with an angle of 45 deg is the ideal case, in which the PLIF data and the gas-sampling data agree with each other perfectly. The open symbols were calculated with the Hartfield method, and the
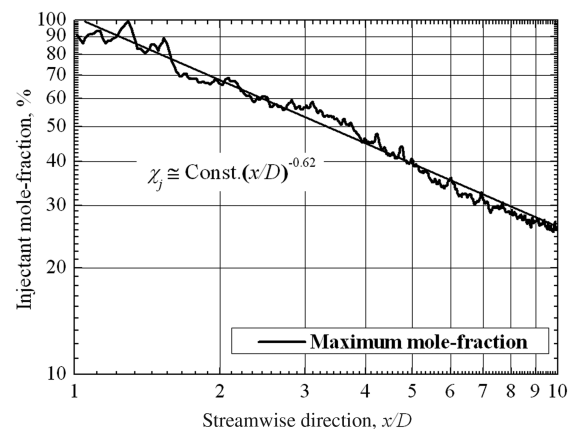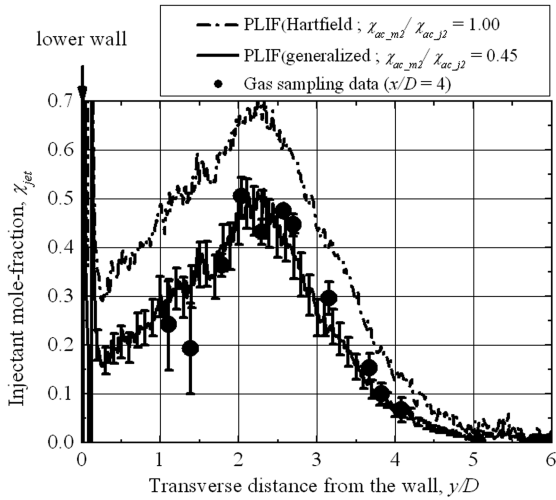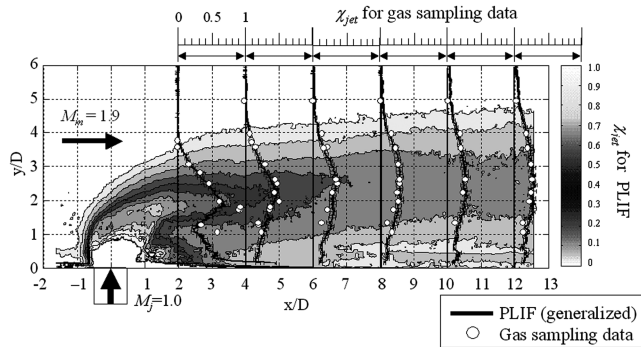

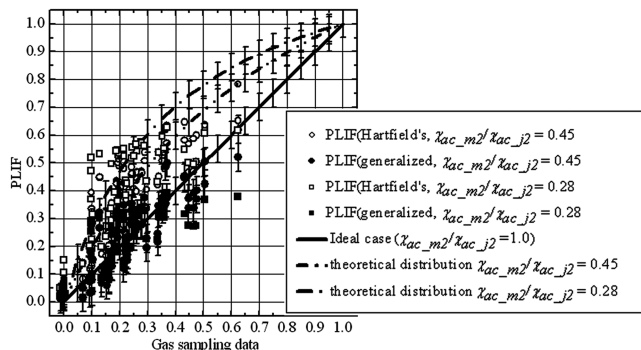Fig. 9   Maximum mole-fraction distribution along the streamwise direction in log–log plot.

Fig. 10 Comparison of PLIF and gas-sampling data containing mole-fraction profiles of $x/D = 4$.

Fig. 11 Comparison of PLIF and gas-sampling data.

solid symbols were calculated with the present generalized method. The circles correspond to $\chi_{ac_{m2}}/\chi_{ac_{j2}} = 0.45$, and the squares correspond to 0.28. The error bars were determined by the uncertainty analysis (i.e., 4.9% for the gas-sampling data and 4.1% for the PLIF data) with both processing methods. Theoretical curves for the Hartfield method with $\chi_{ac_{m2}}/\chi_{ac_{j2}} = 0.45$ and 0.28 calculated from Eq. (8) are also plotted in the figure. The graph clearly indicates that the mole-fraction data obtained with the Hartfield method tends to distribute around the theoretical curves for the corresponding values of $\chi_{ac_{m2}}/\chi_{ac_{j2}}$. In contrast, the present generalized method resulted in better agreement with the ideal line, irrespective of the value of $\chi_{ac_{m2}}/\chi_{ac_{j2}}$. Though the scatter of the generalized data points around the ideal line is relatively large, the generalized fluorescence ratio method presented in this paper results in quantitatively correct mole fractions from the PLIF data.


**Fig. 12 Comparison of mole-fraction value between PLIF and gas-sampling data.**

Figure 13 illustrates the mean cross-sectional mole-fraction distributions at five streamwise locations ($x/D = 0, 4, 8, 12$, and 16). For each cross-sectional plane, images were obtained by averaging 200 instantaneous frames. The reference value for each cross section was determined by taking the maximum mole fraction at each cross section in the center-plane image. Each selected maximum mole-fraction value was confirmed to be the best, because the difference between the mole-fraction profile obtained from the x–y plane and that obtained from the y–z plane rescaled with the reference value was the smallest for each cross-sectional plane. When these cross-sectional images were acquired, a photograph was taken by a camera set to 45 deg against the cross section. The inclined images were corrected to plan-view images in postprocessing. The cross-sectional distributions indicate that a core region of the jet in which no mixing occurred remained for $x/D = 0$ and 4. The plume of injectant became a distinctive horseshoe shape in the downstream region and was completely lifted up from the wall by the section of $x/D = 4$. Splitting or bifurcation of the jet core is observed by $x/D = 8$. The lifted and bifurcated horseshoe shape of the jet plume was produced by a pair of strong counter-rotating streamwise vortices generated downstream of the jet by the injection.

C. Density Distribution

Figure 14 depicts the density distribution derived from PLIF data with Eq. (18). The density distribution was nondimensionalized by the mean density in front of the bow shock wave. We can clearly see the typical flow structures, designated as A to E in Fig. 7b. It is obvious from Eqs. (3) and (4) that the molar concentration (Fig. 7b) is proportional to the product of the density (Fig. 14) and the mole fraction. However, the change in molar concentration is almost proportional to that in density, because the mole fraction hardly changes across the shock waves. The higher-density regions (indicated as bright white regions) that arose from strong compression were observed behind the bow shock, in the periphery of the upstream boundary of the barrel shock, behind the recompression shock, and immediately above the injector exit. In contrast, we observed a lower density than that of the main flow in the recirculation zone downstream of the jet core. Moreover, a gradual decrease of density resulted from the Prandtl–Meyer expansion
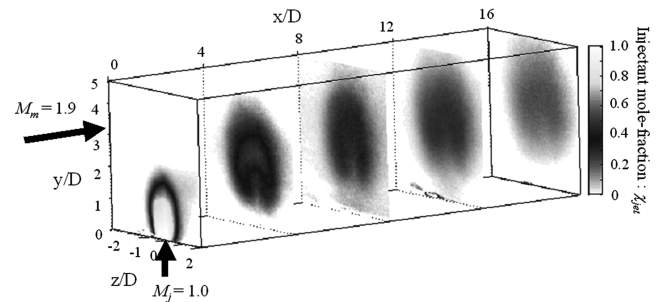
Fig. 13 Injectant mole-fraction distributions in cross-sectional planes.
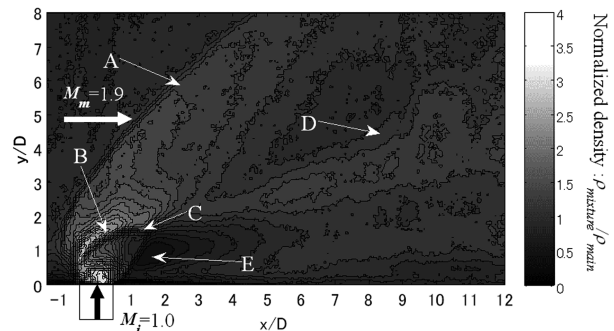
Fig. 14 Normalized density distribution.

occurring inside the barrel shock. These qualitative features are quite reasonable for this kind of supersonic injection flowfield.

Figure 15 plots the distributions of the density ratio across the bow shock along the streamwise direction at $y/D = 3$, 4, 5, 6, and 7. In each profile, the density ratio rapidly increased on passing across the bow shock wave (A); the density then gradually decreased until it increased again by passing the recompression shock wave (D).

Figure 16 compares the theoretical value and the experimental results of the density ratio across the bow shock wave. The theoretical curve was calculated from the oblique shock wave theory with the specific heat ratio of 1.4. The experimental results were obtained with profiles on $3 \le y/D \le 7$ (Fig. 15), because this region was completely above the boundary layer and in the main flow. The boundary-layer thickness was about 5 mm, which corresponds to 2-jet-diameters height from the wall, according to the crossflow velocity profile at $x/D = -2$ separately measured with particle image velocimetry. In Fig. 16, the density ratios at each y position are plotted against corresponding $M \sin(\alpha)$, because the flow conditions behind the bow shock locally hold the oblique shock relationship. Each α was determined by reading shock angles at each y position in Fig. 14. The corresponding Mach numbers at each y position were determined from the velocity profile mentioned earlier. A discrepancy was observed between the theoretical curve and the experimental results, due to the fluctuation of the bow shock wave. Because the bow shock wave was followed by expansion waves, the density distribution had a sharp peak just behind the bow shock

wave. If the position of the bow shock wave fluctuated, the sharp peak of the density distribution would be smeared by averaging. We confirmed that the bow shock position was not kept constant, but fluctuated slightly throughout the experimental runs. As indicated in Fig. 15, every averaged density profile took 1 to 2 mm to rise across the bow shock wave, although it should happen more sharply across the nonfluctuating shock wave. However, the density ratios plotted against the $M \sin(\alpha)$ qualitatively agreed well with each other. Therefore, considering the effect of fluctuation of the bow shock, the density distribution obtained from PLIF with Eq. (18) is appropriate, though the mixing did not quite occur.

V. Conclusions

Hartfield et al.'s fluorescence ratio method [2–7] for imaging the injectant mole fraction was generalized for different rates of seeding fluorescent molecules into the jet and the main stream. Moreover, the method was extended for imaging the local density distributions of the mixture gas. The generalized method was validated by a comparison with the gas-sampling data of the injectant mole fraction. The comparison revealed that the mole fractions obtained with the generalized method agreed better with the gas-sampling data than those obtained with Hartfield et al.'s original method. As for the density distributions, the extended method was well validated by comparison with the theoretical value across the oblique shock wave. The derived density distribution was validated in the region in which mixing hardly occurred. However, the mole-fraction distribution was obtained quantitatively, so that the density in the jet in which the mixing occurred well would be derived as appropriate values.

Fig. 15   Normalized density distribution across the bow shock wave along x axis.

Fig. 16   Comparison of the theoretical curve with the specific heat ratio of 1.4 and the experimental results in density ratio through the bow shock wave.

References

[1] Lozano, A., Yip, B., and Hanson, R. K., "Acetone: A Tracer for Concentration Measurements in Gaseous Flows by Planar Laser-Induced Fluorescence," *Experiments in Fluids*, Vol. 13, No. 6, 1992, pp. 369–379.
doi:10.1007/BF00223244

[2] Hartfield, R. J., Jr., Abbitt, J. D., III, and McDaniel, J. C., "Injectant Mole Fraction Imaging in Compressible Mixing Flow Using Planar Laser-Induced Iodine Fluorescence," *Optics Letters*, Vol. 14, No. 16, Aug. 1989, pp. 850–852.

[3] Abbitt, J. D., III, Hartfield, R. J., Jr., and McDaniel, J. C., "Mole-Fraction Imaging of Transverse Injection in a Ducted Supersonic Flow," *AIAA Journal*, Vol. 29, No. 3, Mar. 1991, pp. 431–435.
doi:10.2514/3.10596

[4] Hartfield, R. J., Jr., Abbitt, J. D., III, and McDaniel, J. C., "Mixing from a Slot Injector in Compressible Flow with an Adverse Pressure Gradient," AIAA Paper 95-0521, Jan. 1995.

[5] Donohue, J. M., McDaniel, J. C., Jr., Haj-Hariri, H., "Experimental and Numerical Study of Swept Ramp Injection into a Supersonic Flowfield," *AIAA Journal*, Vol. 32, No. 9, Sept. 1994, pp. 1860–1867.

[6] Hollo, S. D., McDaniel, J. C., Hartfield, R. J., Jr., "Quantitative Investigation of Compressible Mixing: Staged Transverse Injection into Mach 2 Flow," *AIAA Journal*, Vol. 32, No. 3, Mar. 1994, pp. 528–534.

[7] Hartfield, R. J., Jr., Hollo, S. D., McDaniel, J. C., "Experimental Investigation of a Supersonic Swept Ramp Injector Using Laser-Induced Iodine Fluorescence," *Journal of Propulsion and Power*, Vol. 10, No. 1, Jan. 1994, pp. 129–135.
doi:10.2514/3.23721

[8] Yuen, L. S., Peters, J. E., and Lucht, R. P., "Pressure Dependence of Laser-Induced Fluorescence from Acetone," *Applied Optics*, Vol. 36, No. 15, May. 1997, pp. 3271–3277.
doi:10.1364/AO.36.003271

[9] Koch, U., "Fuel Tracer Photophysics for Quantitative Planar Laser-Induced Fluorescence," Ph.D. Dissertation, Mechanical Engineering Dept., Stanford Univ., Stanford, CA, May 2005.
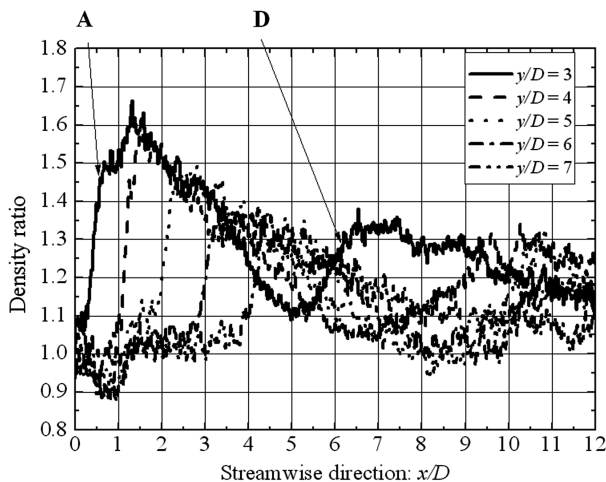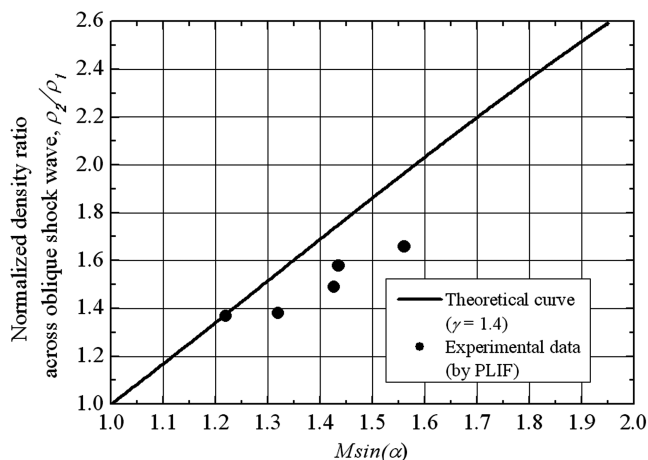
[10] Thurber, M. C., "Acetone Laser-Induced Fluorescence for Temperature and Multiparameter Imaging in Gaseous Flows," Ph.D. Dissertation, Mechanical Engineering Dept., Stanford Univ., Stanford, CA, Mar. 1999.

[11] Takahashi, H., Hirota, M., Oso, H., and Masuya, G., "Measurement of Supersonic Flowfield Using Acetone PLIF," *Journal of the Japan Society for Aeronautical and Space Sciences*, Vol. 55, No. 642, Jul. 2007, pp. 318–323.
doi:10.2322/jjsass.55.318, (in Japanese)

[12] Kashitani, M., Yamaguchi, Y., Handa, T., Masuda, M., Matsuo, K., "A Preliminary Study on Acetone Laser-Induced Fluorescence Technique for Low Temperature Flows," AIAA Paper 2004-385, Jan. 2004.

[13] Wang, K. C., Smith, O. I., and Karagozian, A. R., "In-Flight Imaging of Transverse Gas Jets Injected into Compressible Crossflows," *AIAA Journal*, Vol. 33, No. 12, Dec. 1995, pp. 2259–2263.

doi:10.2514/3.12977

[14] Broadwell, J. E., and Breidenthal, R. E., "Structure and Mixing of a Transverse Jet in Incompressible Flow," *Journal of Fluid Mechanics*, Vol. 148, 1984, pp. 405–412.
doi:10.1017/S0022112084002408

[15] Kouchi, T., Sakuranaka, N., Izumikawa, M., and Tomioka, S., "Pulsed Transverse Injection Applied to a Supersonic Flow," AIAA Paper 2007-5405, Jul. 2007.

[16] Smith, S. H., and Mungal, M. G., "Mixing, Structure and Scaling of the Jet in Crossflow," *Journal of Fluid Mechanics*, Vol. 357, 1998, pp. 83–122.
doi:10.1017/S0022112097007891

R. Lucht
Associate Editor